Appl. Phys. B 87, 221–226 (2007)
DOI: 10.1007/s00340-006-2574-6

Applied Physics B
Lasers and Optics

H. MASHIKO[1,2*]
A. SUDA[1,✉]
K. MIDORIKAWA[1,2]

Second-order autocorrelation functions for all-reflective interferometric autocorrelator

[1] RIKEN, 2-1 Hirosawa, Wako-shi, Saitama 351-0198, Japan
[2] Department of Information and Mathematical Sciences, Saitama University, 255 Okubo, Saitama, Saitama 338-8570, Japan

Received: 5 October 2006/Revised version: 3 November 2006
Published online: 17 February 2007 • © Springer-Verlag 2007

ABSTRACT We investigate the characteristics of an all-reflective interferometric autocorrelator in which the reflective beam splitter has functions as a beam splitter and an optical delay line. Theoretical autocorrelation functions are derived as functions of the beam profile, gap width, and alignment conditions. The results are compared with experiments in order to verify their practical use.

PACS 42.65.Re; 42.65.Tg

1 Introduction

There has been an increase in the use of femtosecond lasers in a variety of fields such as high-field physics, photochemistry, and materials processing. Nowadays, generation of femtosecond laser pulses of less than 5 fs can be achieved in the visible region [1–5]. The measurement of such ultrashort pulses requires robust, high-resolution techniques based preferably on simple principles, such as autocorrelation. We have developed and demonstrated an all-reflective interferometric autocorrelator [6], which has functions as a beam splitter, an optical delay line, and a focusing mirror. The incident beam is separated into two equal parts by the reflective beam splitter and these are superimposed at the focal point. The spatial distribution of the synthesized electric field at the focal point changes depending on the relative phase. Because of its compact and rigid structure, this autocorrelator makes stable and high-resolution measurement possible. Moreover, only one reflection is required in the autocorrelator, which is particularly advantageous for measurements in the XUV and soft X-ray regions. In the visible region, this is suitable for dispersion-less measurement of ultrashort laser pulses.

Some unknown characteristics are derived from the all-reflective interferometer where the autocorrelation signal is generated in a spatially synthesized electric field. For example, the fringe visibility in the measured autocorrelation trace was not as high as in the calculated one as shown in our previous result [6]. We have speculated that the interferometric term in the autocorrelation function is influenced by the spatial profile of the incident beam and the existence of a gap between the two split beams. We also considered that the autocorrelation signal should be generated at the focal point in the case of an all-reflective autocorrelator. Deviation from the focal point would not only degrade the fringe visibility but also the shape of the envelope. This is particularly important when the signal is generated though the interaction of an optical pulse within a volume of nonlinear material. In the short wavelength region below the ultraviolet, there are no $\chi^{(2)}$-based nonlinear crystals, so thicker materials based on $\chi^{(3)}$ nonlinearity, such as fused silica and alkali halide crystals [7, 8], or gaseous medium [9, 10], have to be employed. From this standpoint, the evaluation of autocorrelation signals generated at positions away from the focal point should be investigated together with that for interaction within a volume. Another point to be taken into account is the spatial deviation of the two beams at the focal point. If the two mirrors of the beam splitter are not precisely adjusted in displacement and parallelism, the two beams will not be superimposed at the focal point. Thus, the effects of deviation of the two beams in a lateral direction at the focal point should be examined.

In this paper, we present, in Sect. 2, a theoretical treatment of the autocorrelation functions of an all-reflective interferometric autocorrelator. Section 3 gives the experimental setup and the method used to align the autocorrelator. Section 4 contains the results and discussions on the autocorrelation functions under various conditions. Based on the investigations we evaluate the practicability of the all-reflective interferometric autocorrelator. Section 5 gives our conclusion to this work.

2 Theoretical treatment

The principle of an all-reflective interferometric autocorrelator and an analytical solution of the second-order correlation function were presented in our previous paper [6]. Here, we extend the analytical solution to more general expressions. Figure 1 is a schematic view showing the electric field of two split beams $\tilde{u}_1(x, y)$ and $\tilde{u}_2(x, y)$ and the corresponding focused beams $\tilde{U}_1(x, y)$ and $\tilde{U}_2(x, y)$. We assume that $\tilde{U}_1(x, y)$ and $\tilde{U}_2(x, y)$ are line-symmetric with regard to the y-axis. At the focal point, i.e., $z = f$, $\tilde{U}_1(x, y)$ and $\tilde{U}_2(x, y)$ have the same electric-field profiles, but the wavefronts tilt in

✉ Fax: +81-48-462-4682, E-mail: asuda@riken.jp
*Present Address: Department of Physics, Kansas State University, Cardwell Hall #132 Manhattan, KS 66506, USA

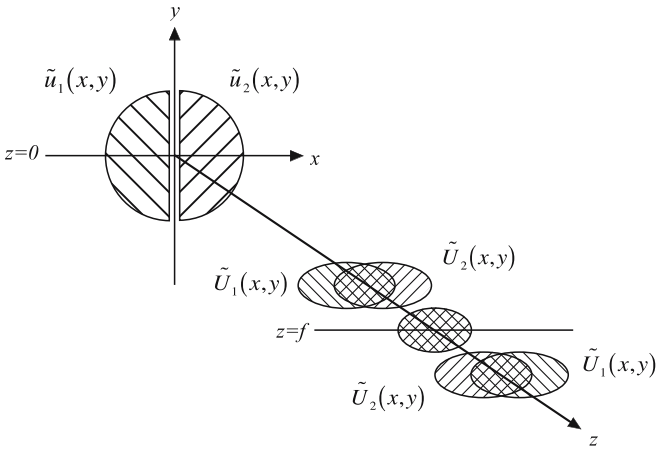

FIGURE 1 Schematic view showing the electric fields of two split beams $\tilde{u}_1(x, y)$ and $\tilde{u}_2(x, y)$ and the corresponding focused beams $\tilde{U}_1(x, y)$ and $\tilde{U}_2(x, y)$

opposite directions to each other, i.e.,

$$\begin{aligned} \left|\tilde{U}_1(x, y)\right| &= \left|\tilde{U}_2(x, y)\right| \\ \varphi_1(x, y) &= -\varphi_2(x, y)\,. \end{aligned} \tag{1}$$

The previous results were based on this assumption. At positions other than the focal point, i.e., $z \neq f$, we can assume that

$$\begin{aligned} \left|\tilde{U}_1(x, y)\right| &= \left|\tilde{U}_2(-x, y)\right| \\ \varphi_1(x, y) &= \varphi_2(-x, y)\,. \end{aligned} \tag{2}$$

The second-order correlation function based on this assumption is given by

$$\begin{aligned} G_2(\tau) =& F_1(\tau) + S_1 F_2(\tau)\cos(\Omega\tau) \\ &+ \{S_3\cos(2\Omega\tau) + S_5\} F_3(\tau)\,, \end{aligned} \tag{3}$$

where Ω and τ are the angular frequency of the pulses and the time delay between two pulses, respectively. The temporal parameters $F_i(\tau)$ $(i = 1\text{–}3)$ and spatial factors S_j $(j = 1\text{–}5)$ are expressed as follows,

$$\begin{aligned} F_1(\tau) &= \int_{-\infty}^{\infty} \mathrm{d}t \left\{ f(t)^4 + f(t-\tau)^4 \right\} \\ F_2(\tau) &= 4\int_{-\infty}^{\infty} \mathrm{d}t \left\{ f(t)\, f(t-\tau) \left[f(t)^2 + f(t-\tau)^2 \right] \right\} \\ F_3(\tau) &= 2\int_{-\infty}^{\infty} \mathrm{d}t \left\{ f(t)^2 f(t-\tau)^2 \right\}, \end{aligned} \tag{4}$$

$$\begin{aligned} S_1 =& \int_{-\infty}^{\infty} \mathrm{d}s \left|\tilde{U}_1(x, y)\right| \left|\tilde{U}_2(x, y)\right| \left|\tilde{U}_k(x, y)\right|^2 \\ &\times \cos(\varphi_1(x, y) - \varphi_2(x, y)) \Big/ \int_{-\infty}^{\infty} \mathrm{d}s \left|\tilde{U}_k(x, y)\right|^4 \end{aligned}$$

$$\begin{aligned} S_3 =& \int_{-\infty}^{\infty} \mathrm{d}s \left|\tilde{U}_1(x, y)\right|^2 \left|\tilde{U}_2(x, y)\right|^2 \\ &\times \cos\left[2(\varphi_1(x, y) - \varphi_2(x, y))\right] \Big/ \int_{-\infty}^{\infty} \mathrm{d}s \left|\tilde{U}_k(x, y)\right|^4 \end{aligned}$$

$$S_5 = 2\int_{-\infty}^{\infty} \mathrm{d}s \left|\tilde{U}_1(x, y)\right|^2 \left|\tilde{U}_2(x, y)\right|^2 \Big/ \int_{-\infty}^{\infty} \mathrm{d}s \left|\tilde{U}_k(x, y)\right|^4, \tag{5}$$

where $f(t)$ is the temporal profile of the pulse envelope. The subscript k may take either 1 or 2. The spatial factors S_2 and S_4 presented in the previous work [6] are omitted here because of the symmetry defined by (2). S_5 is a newly generated factor instead of omitting the $4\, f(t)^2\, f(t-\tau)^2$ term from $F_1(\tau)$.

In this paper, the spatial factors are numerically calculated based on (5) from $\tilde{U}_1(x, y)$ and $\tilde{U}_2(x, y)$, which are obtained by integrating the diffraction equations for $\tilde{u}_1(x, y)$ and $\tilde{u}_2(x, y)$. It should be noted that the results of the numerical calculations show S_3 to be negligibly small. Thus, we can rewrite (3) removing S_3, as follows.

$$G_2(\tau) = F_1(\tau) + S_1 F_2(\tau)\cos(\Omega\tau) + S_5 F_3(\tau)\,. \tag{6}$$

The first and third terms represent the intensity autocorrelation function and the second term forms the interferometric fringes.

3 Experimental setup

Figure 2 shows the experimental setup of the autocorrelator. The beam splitter was made by cutting mirrors from one piece of a flat mirror blank and then coating them with gold. One of these was fixed on a mirror holder and the other on a piezo-electric actuator (PI P-842.10) for the optical delay. This piezo-actuator has a maximum stroke of 12 μm, and a resolution of 1 nm controlled by a feedback system. The gap between the mirrors was 100 μm. The displacement and parallelism were observed using a laser displacement sensor (Keyence LT-8000) and adjusted to be the best possible using manual actuators (Newport HPS-100) attached to the mirror

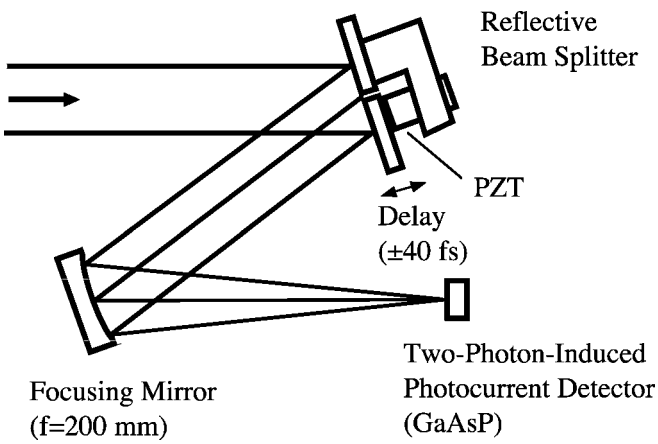

FIGURE 2 Experimental setup for the all-reflective autocorrelator

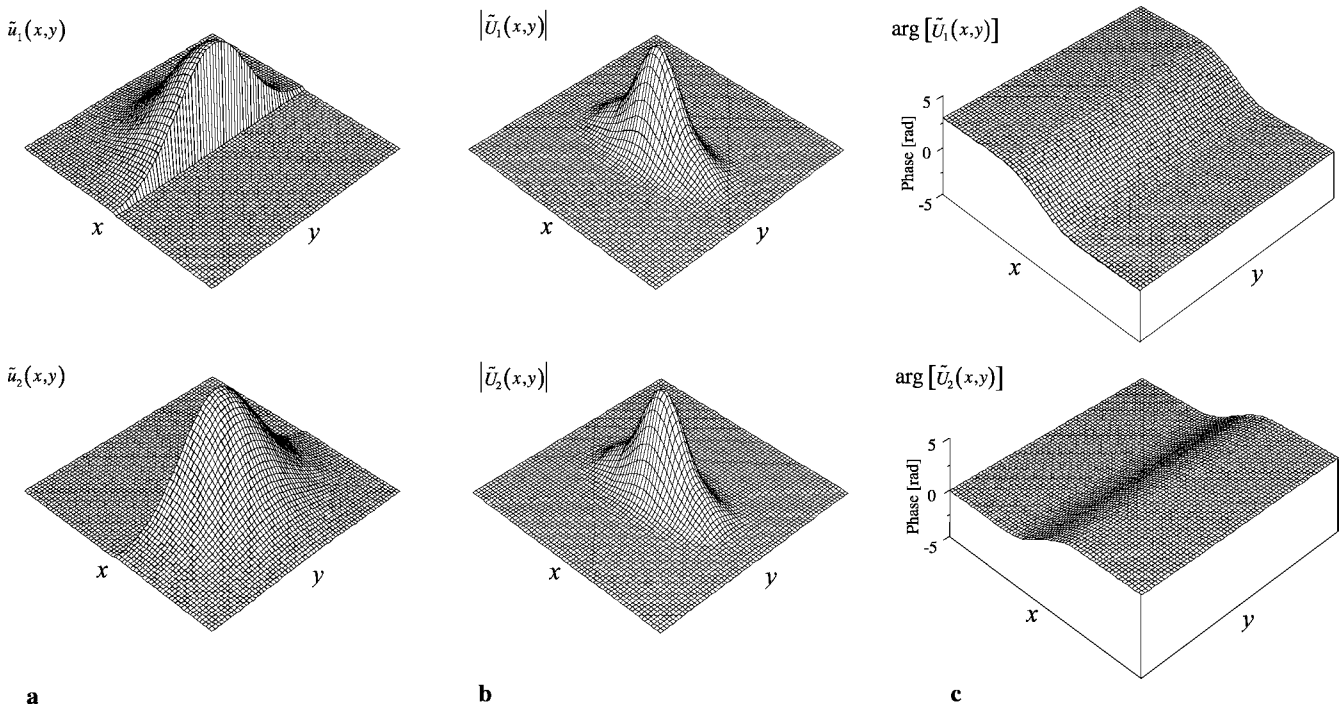

FIGURE 3 Spatial profiles of electric fields (**a**) before focusing and (**b**) at the focal point, and (**c**) phase at the focal point. The initial beam profile assumed is Gaussian

mounts. Thus, this beam splitter is simple in structure, reliable in operation and robust in performance.

The output beam from a mode-locked Ti:sapphire oscillator (14 fs) was sent to the beam splitter. The two beams were focused with a lens of focal length 200 mm and superimposed onto a two-photon induced photocurrent detector (GaAsP), which can detect through the second-order autocorrelation signal. The spot size at the focal point was approximately 17 μm when the beam was not split into two.

4 Results and discussions

4.1 *Effect of gap width and beam profile on the fringe visibility*

Here, the variation of the autocorrelation trace with the gap width and the spatial beam profile is investigated. As an example of the spatial profile, we deal with super-Gaussian functions expressed as

$$E(r) = \exp\left[-(r/r_0)^n\right], \tag{7}$$

where r_0 is the spot size of the beam, r the radial distance, and n the index of super-Gaussian profile. As is well known, $n = 2$ and $n > 2$ correspond to Gaussian and super Gaussian profiles, respectively. The extreme case is a top-hat profile given when n is a large number, e.g., $n = 100$. The spatial profile at the focal point is calculated using the diffraction integral for an initial profile given by (7). Figure 3 shows one of the examples of the spatial profiles (a) initial and (b) at the focal point together with (c) phase at the focal point, where the initial profile assumed is Gaussian. Then, the spatial factors are evaluated using (5) and the calculated spatial profiles. As long as the autocorrelation signal is generated at the focal point $z = f$, S_5 remains constant at 2.0, and the effect of the beam profile appears in the fringe visibility that accompanies the S_1 value. It is noted that the higher the value of S_1 the higher the fringe visibility.

Figure 4 shows the S_1 value as a function of the gap width δ for various values of the super Gaussian index n, where the gap width δ is normalized by the spot size of the incident beam before splitting ω. S_1 takes a maximum value of

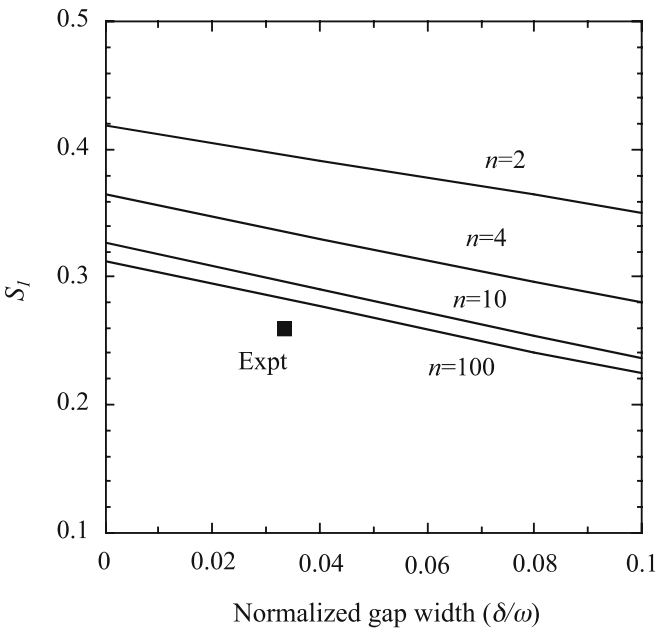

FIGURE 4 The variation in the value of S_1 as a function of gap width for various values of the super Gaussian index n. The plot shows the experimental data

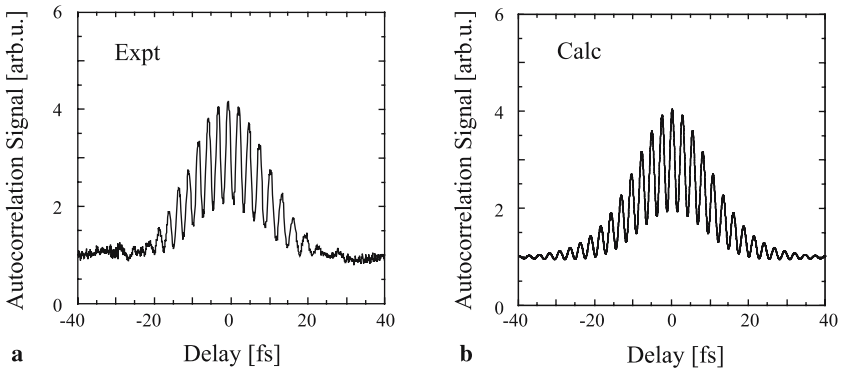

FIGURE 5 (**a**) Experimental and (**b**) calculated autocorrelation traces for a hyperbolic-secant squared temporal profile assuming a pulse width of 14 fs (FWHM)

0.41 for a Gaussian beam without a gap and monotonously decreases with increasing the gap width and increasing n. The plot shows the experimental data obtained from the measured autocorrelation trace in Fig. 5a, where the spatial factor S_1 was evaluated to be 0.26. Compared with the calculated values, S_1 of 0.26 is too low even assuming a top-hat spatial profile. This result suggests the possibility of degradation of the fringe visibility not only by the intensity distribution of the incident beam but also by wavefront distortion of the incident beam. Figure 5b shows a corresponding retrieved trace based on (6) with $S_1 = 0.26$ and $S_5 = 2.0$. The temporal profile assumed here is a hyperbolic-secant squared profile with a full-width at half maximum (FWHM) pulse duration of 14 fs, showing good agreement with the measured autocorrelation trace.

4.2 *Autocorrelation signals generated at positions away from the focal point*

When the signal is generated at positions other than the focal point, S_5 decreases from 2.0, and hence, the envelope of the autocorrelation trace changes somewhat depending on the distance from the focal point. Moreover, the fringe visibility degrades along with a decrease in S_1. Figure 6 shows S_1 and S_5 values as a function of the distance from the focal point Δz, where the distance is normalized by the Rayleigh-length z_R. The initial beam profile assumed here is Gaussian. Because the curves are symmetric before and after the focal point within the region from $\Delta z/z_R = -5$ to 5, we show only half the region in Fig. 6. Based on the S_1 and S_5 values, we compare the calculated autocorrelation traces with those obtained in experiments. Figures 7a and b show autocorrelation traces at a position 1 mm from the focal point, which corresponds to the Rayleigh-length ($\Delta z/z_R = 1$), and Figs. 7c and d show autocorrelation traces at a position 5 mm from the focal point ($\Delta z/z_R = 5$). The autocorrelation trace does not change very much within the Rayleigh-range. At the focal point, the deconvolution factor, which is the ratio of the autocorrelation width (FWHM) to the original pulse width (FWHM), is 1.66 for the hyperbolic-secant squared temporal profile. At $\Delta z/z_R = 1$, the deconvolution factor is 1.63, which differs by only 2%. On the other hand, the autocorrelation trace outside the Rayleigh-range shown in Figs. 7c and d is different than the other two. Overall, good agreement was obtained between the experiment and the calculation.

For interaction in a volume, the spatial factors are obtained by further integrating along the z-axis and are expressed as,

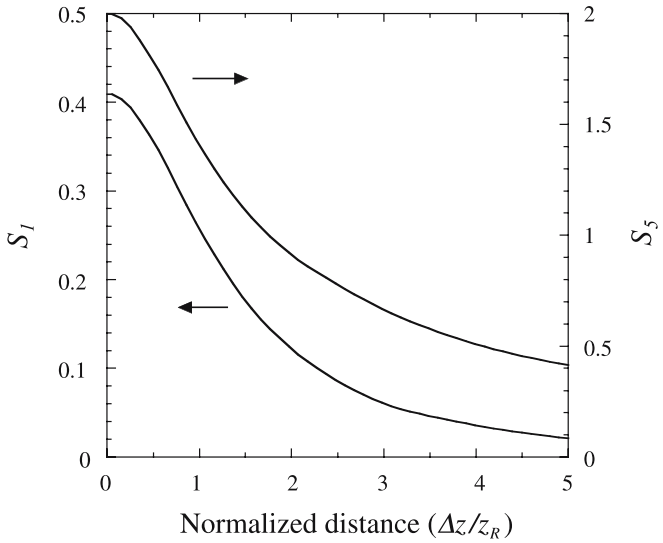

FIGURE 6 The variations in the values of S_1 and S_5 as a function of the distance from the focal point, where the distance is normalized by the Rayleigh-length z_R

$$S_1 = \int_{-\infty}^{\infty} \mathrm{d}V \left|\tilde{U}_1(x,y,z)\right| \left|\tilde{U}_2(x,y,z)\right| \left|\tilde{U}_k(x,y,z)\right|^2 \times \cos(\varphi_1(x,y,z) - \varphi_2(x,y,z)) \Big/ \int_{-\infty}^{\infty} \mathrm{d}V \left|\tilde{U}_k(x,y,z)\right|^4$$

$$S_5 = 2 \int_{-\infty}^{\infty} \mathrm{d}V \left|\tilde{U}_1(x,y,z)\right|^2 \left|\tilde{U}_2(x,y,z)\right|^2 \Big/ \int_{-\infty}^{\infty} \mathrm{d}V \left|\tilde{U}_k(x,y,z)\right|^4 . \quad (8)$$

Numerical integration was made from $\Delta z/z_R = -5$ to 5, where the initial beam profile assumed was Gaussian without a gap. As a result, S_1 and S_5 are 0.27 and 1.48, respectively. It is noted again that S_3 is almost zero and can be neglected. Although the autocorrelation trace for interaction in a volume has not been observed experimentally, we can speculate from the S_1 and S_5 values that it would be almost the same as shown in Fig. 7b. Thus, the autocorrelation signal for interaction in a volume is duly available without serious degradation.

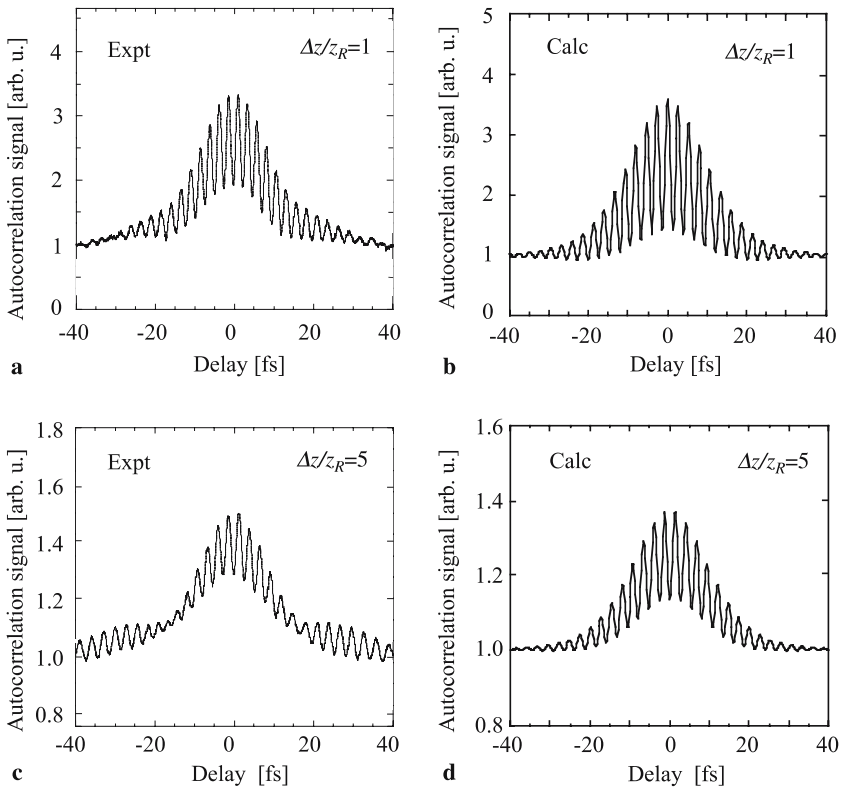

FIGURE 7 (**a**) Experimental and (**b**) calculated autocorrelation traces observed at a position 1 mm from the focal point ($\Delta z/z_R = 1$). (**c**) and (**d**) are the same as (**a**) and (**b**) except that the position is 5 mm from the focal point ($\Delta z/z_R = 5$)

4.3 *Effects of deviation of two split beams in the lateral direction*

We consider here the case in which two beams deviate from each other in the x or y direction at the focal point. The spatial factors S_1 and S_5 are calculated based on (5) and shown in Fig. 8 as a function of the distance between the two beams (a) in the x direction D_x and (b) in the y direction D_y, where the distance is normalized by the spot size of the focused beam ω_0. It is noted again that the initial beam profile assumed here is Gaussian. With increasing either D_x/ω_0 or D_y/ω_0, S_5 decreases much more than S_1. This feature leads to a drastic change in the autocorrelation trace as shown in Fig. 9, where D_x/ω_0 and D_y/ω_0 are set at 3.0 and 0.0, respectively. In typical autocorrelation traces in an all-reflective interferometric autocorrelator, the lower envelope is curved on the upper side. However, it is now curved on the lower side, which is similar to that observed in a Michelson-type interferometer. This kind of waveform appears when the ratio of S_5 to S_1 is lower than 4.0. In Fig. 9, the experimental trace agrees well with calculation. These results show that the autocorrelation trace itself can be a measure of the alignment accuracy.

5 Conclusion

We have studied the characteristics of an all-reflective interferometric autocorrelator for dispersion-less measurement of ultrashort optical pulses. We investigated variations in the autocorrelation traces as a function of gap

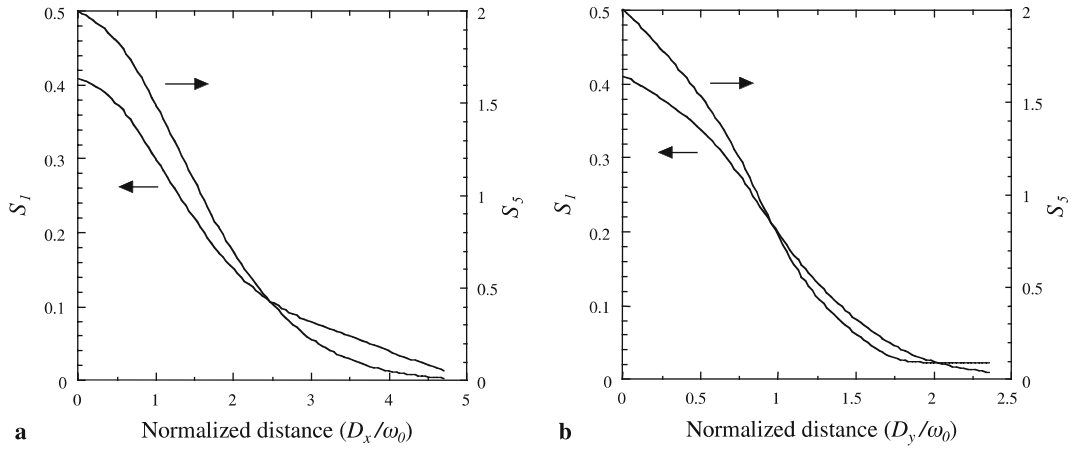

FIGURE 8 The variations in the values of S_1 and S_5 as a function of the distance between two beams at the focal point, where the distance is normalized by the spot size of the focused beam ω_0

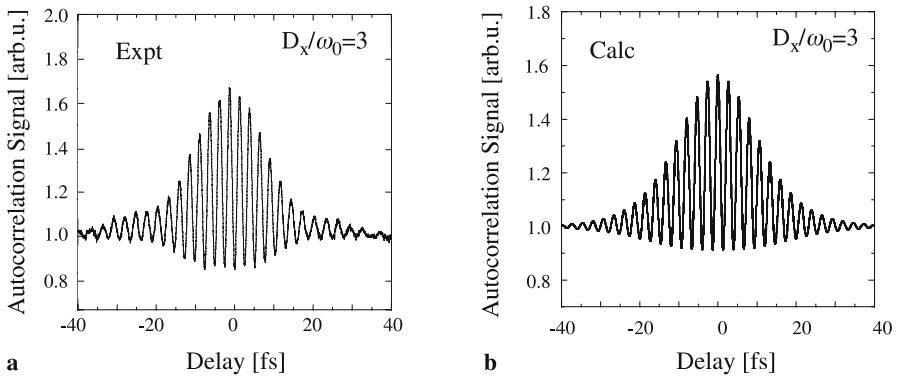

FIGURE 9 (**a**) Experimental and (**b**) calculated autocorrelation traces of two laterally deviated beams ($D_x/\omega_0 = 3$ and $D_y/\omega_0 = 0$)

width, beam profile, observation point, and aberration of the two beams in a lateral direction at the focal point. In all the cases studied here, the autocorrelation traces agree with the calculated traces derived based on spatial factors numerically obtained for various conditions. Although the fringe visibility is reduced depending on the parameters, the deconvolution factor does not show a remarkable change, and hence, the measurement is not seriously degraded.

The all-reflective autocorrelator is effective for the measurement of ultrashort optical pulses in the short-wavelength region, where good optical elements are not available. We also believe that this type of autocorrelator is practical for many applications.

ACKNOWLEDGEMENTS H.M. acknowledges support from the Junior Research Associate Program of RIKEN.

REFERENCES

1 U. Morgner, F.X. Kärtner, S.H. Cho, Y. Chen, H.A. Haus, J.G. Fujimoto, E.P. Ippen, V. Scheuer, G. Angelow, T. Tschudi, Opt. Lett. **24**, 411 (1999)
2 D.H. Sutter, G. Steinmeyer, L. Gallmann, N. Matuschek, F. Morier-Genoud, U. Keller, V. Scheuer, G. Angelow, T. Tschudi, Opt. Lett. **24**, 631 (1999)
3 A. Baltuska, T. Fuji, T. Kobayashi, Opt. Lett. **27**, 306 (2002)
4 N. Zhavoronkov, G. Korn, Phys. Rev. Lett. **88**, 203 901 (2002)
5 S. Sartania, Z. Cheng, M. Lenzner, G. Tempea, C. Spielmann, F. Krausz, K. Ferencz, Opt. Lett. **22**, 1562 (1997)
6 H. Mashiko, A. Suda, K. Midorikawa, Appl. Phys. B **76**, 525 (2003)
7 J.I. Dadap, G.B. Focht, D.H. Reitze, M.C. Downer, Opt. Lett. **16**, 499 (1991)
8 F.G. Omenetto, W.A. Schroeder, K. Boyer, J.W. Longworth, A. Mc Pherson, C.K. Rhodes, Appl. Opt. **36**, 3421 (1997)
9 N.A. Papadogiannis, G. Nersisyan, E. Goulielmakis, T.P. Rakitzis, E. Hertz, D. Charalambidis, G.D. Tsakiris, K. Witte, Opt. Lett. **27**, 1561 (1999)
10 N. Sarukura, M. Watanabe, A. Endoh, S. Watanabe, Opt. Lett. **13**, 996 (1988)